Journal of Materials Chemistry A

Accepted Manuscript

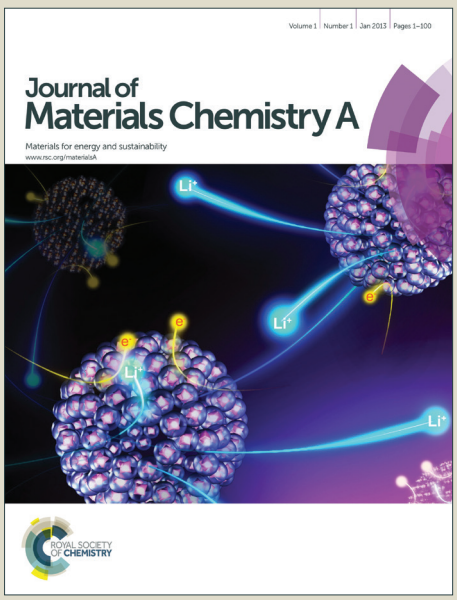

ROYAL SOCIETY OF CHEMISTRY

www.rsc.org/materialsA

Particle-size and morphology dependence of the preferred interface orientation in $LiFePO_4$ nano-particles

Aziz Abdellahi[1], Oncu Akyildiz[2,3], Rahul Malik[1], Katsuyo Thornton[2], Gerbrand Ceder[1].

[1] Department of Materials Science and Engineering, Massachusetts Institute of Technology, Cambridge, MA, USA, 02141

[2] Department of Materials Science and Engineering, University of Michigan, Ann Arbor, MI, USA, 48109

[3] Department of Metallurgical and Materials Engineering, Hitit University, Corum, Turkey

E-mail : gceder@mit.edu

Abstract

We gain new insights into the equilibrium properties and potential two-phase lithiation mechanisms in $LiFePO_4$ nano-particles by conducting a first-principles investigation of the anisotropic chemical interfacial energy landscape in $LiFePO_4$. The chemical interfacial energy per unit area along the *ac* plane is found to be remarkably low (7

mJ/m^2) with respect to the *bc* (115 mJ/m^2) and *ab* (95 mJ/m^2) chemical interfacial energies. Because chemical interfacial energy and coherency strain energy have different anisotropies, the thermodynamically stable interface orientation is shown to depend both on the particle size and on the particle morphology. In particular, *ac* interfaces are favored for isotropic particles below 40 nm. This indicates that, if experimentally-relevant nano-particles were to (de)lithiate under a thermodynamic two-phase mechanism, the resulting front would be orientated along the *ac* plane, and not along the *bc* plane as is assumed in most lithiation models in the literature.

Introduction

$LiFePO_4$ is an important commercial cathode material for Li-ion batteries due to its safety [1], reasonable energy density (170 mAh/g, 3.4 V vs. Li^+/Li)[2], and high rate capability. Capacities as high as 130 mAh/g have been achieved at 50 C rate ((dis)charge in 72s), and rates as high as 200 C and 400 C ((dis)charge in 18s and 9s respectively) have been achieved by removing kinetic limitations at the electrode level. [3-7] These high rates are achievable only when the particle size is reduced to the nano-scale (~ 50 – 100 nm) [3-7], a phenomenon that has been attributed in part to reduced Li mobility due to channel-blocking anti-site defects in larger particles.[8-10] However, the mechanism by which pristine nano-sized particles achieve high rates is still debated in the $LiFePO_4$ literature.

Several models have been proposed to explain the (de)lithiation mechanisms in $LiFePO_4$ single particles by taking into account the two-phase nature of bulk Li_xFePO_4.

[2,11-17] Among these models, a large fraction operates under one or both of the following assumptions:

1) (De)lithiation is initiated by a nucleation event[2,12,15,16,18]

2) Phase transformation proceeds through the propagation of a *bc* phase front[11,12,15,16].

The nucleation assumption is generally accepted, as it describes the phase transformation kinetics of a large fraction of two-phase systems[19]. Several authors, on the other hand, have argued against the possibility of high-rate nucleation and have proposed a non-equilibrium solid solution mechanism as an alternative[16,17,20]. The *bc* phase boundary assumption is justified by the minimization of the lattice mismatch in the plane of the interface (the lattice mismatch between the $LiFePO_4$ and $FePO_4$ phases is 5.3% in the *a* direction, 3.8% in the *b* direction, and 1.9% in the *c* direction[21]) and has been supported by several observations of *bc* interfaces in ex situ chemically delithiated particles[11,13,22] .

The *bc* phase boundary assumption, although widely accepted in the literature, has recently been questioned by experimental observations[23-26]. Observations on single nano-sized particles have shown that the *bc* plane is not always the preferred boundary orientation in $LiFePO_4$ single particles. Several TEM measurements have in fact demonstrated that the phase orientation depends both on the particle size and on the particle morphology. Specifically :

- By observing preferential fracture planes after electrochemical cycling of spherical 200 nm particles, Gabrisch *et al*.[23] showed the existence of phase boundaries on both the *bc* and *ac* planes.
- Park *et al*.[24] observed only *ac* interfaces in chemically delithiated 100 nm particles.
- Suo *et al*.[25] observed *ab* interfaces after chemical delithiation of 200 nm particles (a ~2 nm region of ordered "staging" was also observed between the two phases).
- Zhu et al observed the propagation of an *ac* interface using in situ TEM on micron sized particles. [26]
- Other interface orientations have also been observed, such as the (101) interface by Ramana et al. [13] and the (110) interface by Laffont et al.[22]

Despite the importance of the *bc* phase front assumption in the $LiFePO_4$ literature, no comprehensive theoretical study has been conducted to verify its validity. In principle, the preferred interface orientation in a single particle can indeed depend both on the particle size and on the particle morphology. Chemical interfacial energy and coherency strain energy scale differently with particle size (the former being proportional to the interfacial area and the latter to the particle volume) and may each favor different interface orientations. The interface orientation that minimizes the coherency strain energy (typically believed to be the *bc* interface) may not always coincide with the interface orientation that minimizes the chemical interfacial energy, thus creating a particle size and morphology dependence of the preferred interface. Understanding the orientation dependence of both the chemical interfacial energy and the coherency strain energy is therefore crucial to determining the preferred phase boundary orientation in

$LiFePO_4$ as a function of the particle size and morphology. Although the effect of anisotropic coherency strain energy has been studied in detail[15,27,28], comprehensive studies of orientation-dependent chemical interfacial energies in conjunction with coherency strain energy have not yet been undertaken.

In this work, we evaluate the validity of the *bc* phase front orientation assumption by comparing the relative stability of the *bc*, *ac* and *ab* interfaces as a function of particle size and mophology, using chemical interfacial energies based on first principles and coherency strain energies based on continuum elasticity. The results of this study will be used to understand the origin of the particle-size and particle-morphology dependence of the preferred interface in $LiFePO_4$ single particles. In particular, the preferred phase front orientation of experimentally relevant sub-50 nm $LiFePO_4$ particles will be investigated, to gain insights on the potential two-phase lithiation mechanisms in nano-$LiFePO_4$ electrodes.

Methodology

An important assumption that will be made throughout this work is the coherent nature of the $FePO_4$/$LiFePO_4$ interface. This assumption is based on two considerations. First, incoherent or semi-incoherent interfaces are known to propagate slowly, as they require the displacement of all atoms of the interface as opposed to only the lithium. This would therefore be inconsistent with the high rates observed in $LiFePO_4$. Second, (semi)incoherent interfaces are known to have a higher chemical interfacial energy than

coherent interfaces and are therefore energetically unfavorable at small particle sizes. We will also assume that the interface is sharp (i.e., the solubility in each phase is negligible and no ordered states exist between the two phases[25]). Although a large fraction of ex situ[11,13,22,23,24] and in situ[26] observations in the $LiFePO_4$ literature are consistent with this assumption, it is important to mention that intermediate solid solution phases at an $FePO_4/LiFePO_4$ interface have also been observed in recent ex situ[25,29] and in situ[30] experiments. The origin of these intermediate solid solution states have been argued to be either of kinetic nature (out of equilibrium Li insertion) or of thermodynamic nature (partial release of coherency strain energy at the interface). Although only sharp interfaces will be considered in this study, a subsequent analysis of the coherency strain energy profile at a sharp $FePO_4/LiFePO_4$ interface will allow us to determine if a thermodynamic driving force to form an intermediate solid solution region at the interface does indeed exist (see Discussion for more details).

The total energy penalty for intra-particle phase-separation (with respect to interparticle phase separation) is the sum of the chemical interfacial energy, which scales as the area of the $LiFePO_4/FePO_4$ interface, and the coherency strain energy, which scales as the particle volume. This dependence is expressed in equation (1).

$$E_{phase-separation} = A_{\text{interface}}\gamma + V_{\text{particle}}e_{strain} \quad (1)$$

In equation (1), $A_{\text{interface}}$ is the interfacial area, γ is the (coherent) chemical interfacial energy per unit area, V_{particle} is the particle volume and e_{strain} is the volume-averaged

coherency strain energy density. More specifically, the quantity e_{strain} is equal to the total strain energy in the particle divided by the total volume of the particle, as expressed in equation (2).

$$e_{strain} = \frac{1}{V_{particle}} \int_{V_{particle}} \frac{1}{2} \sigma_{ij} \varepsilon_{ij}^{elastic} \, dV \qquad (2)$$

In equation (2), σ_{ij} is the stress tensor, $\varepsilon_{ij}^{elastic}$ is the elastic strain tensor, defined as the difference between the total strain tensor and the stress-free strain tensor (see Appendix for more details).

The dependence of the preferred interface orientation on particle size and shape can be explained by the different size-scaling of the chemical interfacial energy and coherency strain energy contributions to the energy penalty for intra-particle phase-separation. While both chemical interfacial energy and coherency strain energy depend on the orientation of the phase boundary, they scale differently with particle size. Chemical interfacial energy scales with the area of the $LiFePO_4/FePO_4$ interface, while coherency strain energy scales with the particle volume. The effect of the chemical interfacial energy is expected to dominate at small sizes, while the effect of the coherency strain energy is expected to dominate at large particle sizes. These different scalings can lead to a particle-size and particle-morphology dependence of the preferred interface orientation, as the interface orientation that minimizes chemical interfacial energy may not coincide with the interface orientation that minimizes coherency strain energy.

The volume-averaged coherency strain energy density e_{strain} is calculated using continuum elasticity models while the chemical interfacial energy per unit area γ is calculated using Density Functional Theory (DFT). A more detailed explanation of these two methods follows.

Chemical interfacial energies per unit area are calculated using the Generalized Gradient Approximation (GGA+U) to Density Functional theory (DFT) as implemented in the Vienna Ab Initio Simulation Package, with a self-consistent U value for Fe of 4.3 as previously determined by Zhou et al.[31] Energies of supercells containing pure $LiFePO_4$, pure $FePO_4$ and an $LiFePO_4/FePO_4$ interface are calculated and their difference is divided by the area of the $LiFePO_4/FePO_4$ interface to obtain the chemical interfacial energy per unit area. This standard procedure is illustrated in equation (3). (Note that, in equation (3), the two-phase supercell contains an equal fraction of each phase.)

$$\gamma_{coherent} = \lim_{N\to\infty} \frac{\left[E^{2-phase}_{N\ unit\ cells} - \frac{N}{2}E^{FePO_4} - \frac{N}{2}E^{LiFePO_4}\right]_{\text{Fixed lattice parameters along the interface plane}}}{2A_{\text{interface}}} \quad (3)$$

Energy calculations of the fully lithiated, fully delithated, and two-phase states are performed at the same lattice parameters along the plane of the interface, while the dimension perpendicular to the interface is allowed to relax. This standard procedure is essential to capture only the chemical interfacial energy component of the energy penalty for phase-separation, without any contribution from the coherency strain energy. In

general, the exact values of the lattice parameters along the interface depend on the relative phase fraction of the $FePO_4$ and $LiFePO_4$ phases. In the extreme cases, an $FePO_4$ nucleus forming in an $LiFePO_4$ matrix will be constrained to the lattice parameters of the $LiFePO_4$ phase, while the opposite applies to an $LiFePO_4$ nucleus in a $FePO_4$ matrix. When the phase fractions are comparable, the lattice parameter at the interface takes a value intermediate to the lattice parameters of the two phases. Since it was found that the calculated chemical interfacial energy per unit area has a weak dependence on the choice of these lattice parameters (e.g. $\pm$ 0.5 mJ/m^2 for the *ac* interface), only the average values obtained at the $FePO_4$ and $LiFePO_4$ lattice parameters will be reported.

The energy cutoff used in each DFT calculation is 520 eV, while the k-points mesh density is $0.3A^{-1}$. All calculations were performed in the ferromagnetic state, following previous studies[20,32]. The ground state Fe^{2+}/Fe^{3+} ordering at the $LiFePO_4/FePO_4$ interface was identified for each interface orientation. Using the linear interpolation method of Fiorentini and Methfessel[33,34], γ values were found to converge at a supercell size consisting of three unit cells of each phase (*N=6* in equation (3)). All the calculation parameters stated above ensure that the reported γ values are converged to within 1 mJ/m^2. The calculated lattice parameters of the pure $FePO_4$ and the $LiFePO_4$ phases, at which the chemical interfacial energies are calculated, are given in and are consistent with previous reports[27].

Table 1. Calculated lattice parameters for the $LiFePO_4$ and $FePO_4$ phases

	a (A^0)	b (A^0)	c (A^0)
$FePO_4$	9.98	5.92	4.88
$LiFePO_4$	10.44	6.07	4.75

At the particle scale, coherency strain energies are calculated using the standard equations of the theory of linear elasticity: mechanical equilibrium, strain compatibility and the linear stress-strain relationship (see Methods section for details). In addition to these standard relations, a continuity condition of the displacements at the $LiFePO_4/FePO_4$ interface is imposed, thus reflecting the fact that the interface is coherent. A traction-free boundary condition is also imposed at the external surfaces of the particle. The latter condition is critical, as it allows stress relaxation via volume expansion/contraction at the particle surface and therefore leads to significantly smaller coherency strain energies than if the entire particle were elastically strained.

Values of the elastic constants for the $LiFePO_4$ and $FePO_4$ phases are taken from the first principles calculations of Maxisch et al.[27] The equations of continuum elasticity are cast into the smoothed boundary method as formulated by Yu *et al*.[35] to solve for the elastic stress tensor and strain tensor using the alternative direction iterative (ADI) method in a second-order central-difference scheme in space. The volume-averaged coherency strain energy density is then calculated from equation (2).

Due to the assumptions of linear elasticity, the volume-averaged coherency strain energy density as defined in equation (2) depends only on the lithium concentration x_{Li}, the interface orientation and the particle morphology, but not on the particle volume (at a given particle morphology). In other words, the total coherency strain energy E_{strain} can be written (equation (4)):

$$E_{strain} = V_{particle} \bullet e_{strain}\left(x_{Li}, \text{interface orientation}, \text{particle morphology}\right) \quad (4)$$

For example, all cubic particles with $x_{Li}=0.5$ and an interface in the *bc* plane have the same volume-averaged coherency strain energy density e_{strain} , regardless of the dimensions of the cube. In this study, only cuboid particles of dimensions L_a x L_b x L_c are considered. One length parameter is used to describe the size of the particles (the dimension perpendicular to the interface, e.g. L_b for *ac* interfaces), while two length ratios are used to describe the morphology of the particles (the ratios of the dimensions parallel and perpendicular to the interface, e.g. L_b / L_a and L_b / L_c for *ac* interfaces).

Results

Table 2 presents the chemical interfacial energies per unit area (excluding coherency strain energy) that were calculated using DFT.

Table 2. Calculated chemical interfacial energies per unit area

***bc* interface**	**ac interface**	**ab interface**
115 mJ/m^2	7 mJ/m^2	95 mJ/m^2

An important consequence of the values reported in **Table 2** is that the chemical interfacial energy landscape is highly anisotropic. The relationship between the magnitudes of the various chemical interfacial energies per unit area is expressed in equations (5).

$$\gamma^{ac} << \gamma^{ab} < \gamma^{bc} \quad (5)$$

The order of magnitude of the calculated chemical interfacial energies per unit area are inconsistent with the 960 mJ/m^2 reported using previous ab initio calculations[36]. The latter value does not seem realistic however, as it is higher than the surface energy of $LiFePO_4$ in the (100) direction and would therefore lead to particle fracture[37]. Our calculated values are also consistent with the general order of magnitude of coherent chemical interfacial energies per unit area, which are known to be on the ~100 mJ/m^2 scale[19], with the exception of γ_{ac} which is found to be exceptionally low. We note that

our values are also closer to the isotropic value of 39 mJ/m^2 recently used in phase field models[38].

The low chemical interfacial penalty along the *ac* plane is consistent with the formation energy of key ordered solid solution states in the Li_xFePO_4 system. Figure 1 shows the energy of various solid solution configurations in Li_xFePO_4 as calculated by Zhou et al[32], among which two have been highlighted. The first ordered configuration consists in a sequence of alternately lithiated and delithiated *bc* planes (referred to as "bc staging" by Zhu et al[20], which we will refer to as "*bc* ordering"), while the second configuration consists in a sequence of alternately lithiated and delithiated *ac* planes (which we will refer to as "*ac* ordering"). These orderings are purely comprised of $LiFePO_4/FePO_4$ interfaces and are therefore key in understanding the origin of the low *ac* chemical interfacial energy with respect to the *bc* chemical interfacial energy. The *ac* ordering, which was shown by Malik et al to be along the path of the low-energy non-equilibrium free energy curve[17], has a formation energy of 10 meV per formula unit of Li (f.u.). By comparison, the *bc* ordering[25] was calculated by Zhu et al[20] to have a positive energy penalty of 70 meV/f.u. The fact that it has been observed experimentally was argued to be either due to kinetic stabilization[20] or to relieve stress along a sharp *ab* interface[25]. Taking into account the fact that the energy penalty for the *ac* ordering state is 7 times lower than that for the *bc* ordering, and taking into account the fact that the interfacial area per formula unit along the *ac* plane is approximately twice that along the *bc* plane (the lattice parameters approximately being *a=10.4 A*, *b=6.1 A*, *c=4.8 A* for $LiFePO_4$), a rough estimate indicates that γ_{ac} should be approximately 14 times lower than γ_{bc} .

Using this ratio to calculate γ_{ac} based on the value of γ_{bc}, we find that this simple model gives an approximate value of $\gamma_{ac}=10\ mJ/m^2$, which is very close to the calculated value. The relative energies of *bc* and *ac* microscopic orderings are therefore consistent with the relative values of the *ac* and *bc* chemical interfacial energies per unit area.

By virtue of equation (1), the low value of γ_{ac} means that the majority of the energy penalty associated with an *ac* interface lies in the coherency strain energy, with only a small contribution from the chemical bonds at the interface. Figure 2 illustrates this fact by comparing the energies of the three configurations that were used to calculate γ_{ac} : a two-phase $LiFePO_4/FePO_4$ supercell, a pure $LiFePO_4$ supercell and a pure $FePO_4$ supercell (all three under the lattice parameters of $LiFePO_4$ for the purposes of this example). Consistent with the phase-separating character of the Li_xFePO_4 system, all three formation energies are greater or equal to zero. The dashed line in Figure 2 (linear interpolation between the energy of the $LiFePO_4$ and strained $FePO_4$ phases) represents the energy penalty only due to coherency strain. The actual formation energy of the two-phase state is higher than the dashed line by a quantity that is proportional to γ_{ac}. This quantity is found to be small for an *ac* interface, thus leading to a low value of γ_{ac} (7 mJ/m^2).

In order to fully characterize the energy penalty for phase-separation, both the chemical interfacial energy and the strain energy resulting from the coherency strain at the interface must be considered. Figure 3 presents the local coherency strain energy density calculated in cubic particles for *ac*, *bc* and *ab* interfaces. In this figure, the

$LiFePO_4/FePO_4$ interface located in the center of the particle, corresponding to an overall composition of $x_{Li}=0.5$ at the particle level.

Because of stress relief at the external surface, elastic strain is limited to a small region around the interface, as illustrated in Figure 3. The length of the strained region is on the order of 10-20% of the particle length, and the maximal local strain energy density in that region is on the order of 30-70 MJ/m^3, depending on the interface orientation. The local coherency strain energy distribution in the particle can be integrated to obtain the volume-averaged coherency strain energy density (total coherency strain energy divided by total volume) as reported in equation (2). The volume-averaged coherency strain energy density can then be calculated as a function of the lithium concentration in the particle by varying the position of the interface, as illustrated in Figure 4.

Figure 4 shows that the volume-averaged coherency strain energy density profile is relatively independent of the volume fraction of the particle that is transformed. This is a consequence of the fact that coherency strain energy is only localized around the interface. A departure from the plateau value occurs when the distance between the interface and the external surface is on the same order of magnitude as the length of the strained region, which corresponds to concentration values close to $x_{Li}= 0$ and $x_{Li}= 1$. The plateau value of the volume-averaged coherency strain energy density is lowest for the *bc* interface ($e^{bc}_{strain} = 3.7\ MJ/m^3$) and largest for the for the *ab* interface ($e^{ab}_{strain} = 9.6\ MJ/m^3$). The *ac* interface has an intermediate value ($e^{ac}_{strain} = 6.5\ MJ/m^3$). Thus :

$$e_{strain}^{bc} < e_{strain}^{ac} < e_{strain}^{ab} \quad \text{(Cubic particles)} \tag{6}$$

This is in agreement with the common assumption that *bc* interfaces minimize coherency strain energy.

For the remainder of this study, only the plateau value of the volume-averaged strain energy density will be stated. This approximation is valid when the phase fraction of the minority phase is sufficiently high (~10-20%). In this regime, Li concentration dependencies can be neglected, such that the dependence on x_{Li} in equation (4) can be discarded.

The total energy penalty for phase-separation in cubic particles can be calculated by combining chemical interfacial energy and coherency strain energy as in equation (1). Figure 5 shows the total energy penalty for phase-separation normalized by the particle volume for cubic particles with sizes ranging from 10 to 110 nm.

A general feature that can be noted from Figure 5 is that the energy for intra-particle phase-separation, when normalized by the particle volume, decreases with particle size for any interface orientation. This is because the interface to volume ratio decreases, thus reducing the relative contribution of the chemical interfacial energy to the total energy penalty for phase-separation. Figure 5 demonstrates that the favored interface orientation depends on the size of the particle. At small particle sizes, an *ac* interface is energetically favorable. Chemical interfacial energy indeed dominates at small particle sizes, thus

favoring *ac* interfaces by virtue of equation (5). At large particle sizes, a *bc* interface is energetically favorable because the coherency strain energy, which is lowest for *bc* interfaces (equation (6)), dominates. The crossover happens at particle sizes on the order of 40 nm. For cubic particle sizes below 40 nm, the favored boundary orientation is therefore *ac*, as opposed to *bc* which is assumed by most lithiation models in the literature [11,12,15,16] .

Up to this point, we have only considered cubic particles. For non-cubic morphologies, in which the dimensions of different interfaces are different, both the chemical interfacial energy and the coherency strain energy will depend on the particle morphology, as expressed in equation (7).

$$E^i_{phase-separation} = A^i\gamma^i + Ve^i_{strain}\left(\text{particle morphology}\right). \quad (7)$$

The chemical interfacial energy penalty for interface i, $A^i\gamma^i$, depends on the particle morphology through the surface scaling A^i. For non-cubic morphologies, the difference in surface area between different interface orientations can make interfaces with large γ^i more favorable if their associated interfacial area A^i is small. This is not the case for cubic morphologies, where all three interface orientations have the same interfacial area. Coherency strain energy also depends on the particle morphology. Coherency strain energy is minimized when the direction perpendicular to the interface, over which coherency stress is allowed to relax, is smaller than the dimensions of the interface, where coherency stress is created. For example, for an interface located in the *bc* plane,

the coherency strain energy will depend on the L_b / L_a and L_c / L_a ratios, with L_a being the direction perpendicular to the interface and L_b and L_c being the dimensions parallel to the interface. The value of e_{strain} decreases as these ratios decrease.[28] It is important to emphasize that, for a given particle morphology (i.e., at fixed L_b / L_a and L_c / L_a ratios in the previous example), the value of the volume-averaged quantity e_{strain} is independent of the volume of the particle, as expressed in equation (7).

The particle-morphology dependence of the chemical interfacial energy and coherency strain energy can be illustrated in a specific subspace of particle morphology, by fixing $L_a = L_c$ and varying the morphology ratio L_b / L_a. According to the value of L_b / L_a , this subspace spans *ac*-platelet particles ($L_b / L_a << 1$, $L_a = L_c$), cubic particles ($L_b / L_a = 1$, $L_a = L_c$) and b-needle particles ($L_b / L_a >> 1$, $L_a = L_c$), as illustrated in Figure 6. Figure 7(a) shows the variation of the total chemical interfacial energy along that subspace (normalized by the particle volume, i.e $A\gamma / V$), while Figure 7(b) and (c) show the variation of the volume-averaged coherency strain energy density e_{strain} and the total energy penalty for phase-separation along that same subspace. In Figure 7, the value of L_b is fixed to 50 nm.

The trends in the chemical interfacial energy penalty $A\gamma / V$ observed in Figure 7(a) can be readily explained by considering the relative difference between the *bc*, *ac* and *ab* interfacial areas along the morphology subspace under consideration. As the L_b / L_a ratio is increased from a value of 0.5 to a value of 2, the area of the *ac* interface relative to the total volume of the particle decreases, while the areas of the *bc* and *ab* interfaces

increase. The relative stability of the *ac* interface is therefore more significant for small L_b / L_a ratios than for large L_b / L_a ratios.

Similarly, the trends in the volume-averaged coherency strain energy e_{strain} (Figure 7(b)) can be explained by considering how the dimensions parallel and perpendicular to the interface vary as the L_b / L_a ratio is increased. The volume-averaged coherency strain energy density associated with an *ac* interface decreases as the L_b / L_a ratio is increased, because the dimension perpendicular to the interface (L_b) is reduced with respect to the dimensions parallel to the interface (L_a and L_c). The opposite applies for *bc* and *ab* interfaces, for which the dimension perpendicular to the interface (L_a and L_c, respectively) decreases with respect to one of the dimensions parallel to the interface (L_b) . As a result, while cubic and ac-platelet morphologies favor *bc* interfaces, *ac* interfaces become favorable for b-needle morphologies.

The previous considerations can be combined to determine the preferred interface orientation as a function of both particle size and particle morphology. These relationships are presented in the form of "interface orientation maps", which illustrate the preferred interface orientation for particles of different sizes in a given morphology subspace. Figure 8 illustrates three examples of such interface orientation maps. Figure 8(a) presents the same morphology subspace as discussed in Figure 6 and Figure 7 ($L_a = L_c$, L_b / L_a allowed to vary), while Figure 8(b) and (c) present the morphology subspaces respectively characterized by $L_b = L_c$ and $L_a = L_b$. The interface orientation maps reported

here constitute a qualitative interpolation based on a discrete set of calculated morphologies.

The results from Figure 8(a) are a direct consequence of the change in the dominant contribution to the energy penalty with the particle size (Figure 5) and particle morphology (Figure 7). A horizontal cut at $L_b / L_a = 1$ in Figure 8(a) corresponds to an analysis of the size dependence of the preferred interface in cubic particles, as was illustrated in Figure 5. In that analysis, it was seen that particles smaller than 40 nm favor *ac* interfaces, while particles larger than 40 nm favor *bc* interfaces. A vertical cut at $L_b = 50\ nm$ in Figure 8(a) corresponds to the morphology dependence of the preferred interface at a fixed particle size of $L_b = 50\ nm$, as was previously illustrated Figure 7(c). In that analysis, it was seen that low L_b / L_a ratios favor *bc* interfaces, while high L_b / L_a ratios favor *ac* interfaces, with a transition between the $L_b / L_a = 1$ and $L_b / L_a = 2$ ratios.

An interesting consequence of the interface orientation map in Figure 8(a) is that, for b-needle particles with an L_b / L_a ratio on the order of 2 or higher, *ac* is the favored interface orientation at all particle sizes. Conversely, as the L_b / L_a ratio is decreased from 1 (cubic morphology) to lower values (ac-platelets), the *ac* interface is favored over smaller and smaller ranges of particle sizes, until the range becomes negligible.

Figure 8(b) and (c) give interface orientation maps for two additional geometry subspaces, corresponding to $L_b = L_c$ and $L_a = L_b$ respectively. Figure 8(c) demonstrates that, in addition to the *bc* and *ac* interfaces, *ab* interfaces can also be favorable at certain

particle sizes and morphologies. In particular, particles with a morphology ratio of $L_c / L_a = 2$ favor *ab* interfaces in the 50 nm-130 nm range. This can be rationalized by considering that *ab* interfaces have a smaller interfacial area than *ac* or *bc* interfaces in that specific particle morphology.

Summary and Discussion

Per unit area, the *ac* chemical interfacial energy (7 mJ/m^2) was shown to be much lower than the *ab* and *bc* chemical interfacial energies (95 mJ/m^2 and 115 mJ/m^2). The exceptionally low value of γ_{ac} was shown to be consistent with the formation energy of key ordered solid solution states, indicating that the chemical penalty to form an interface along an *ac* plane is much lower than along a *bc* or *ab* plane. Because the interface orientation that minimizes the chemical interfacial energy per unit area (*ac*) is not the same as the interface orientation that minimizes the volume-averaged coherency strain energy density (*bc* for cubic particles), the preferred interface orientation in $LiFePO_4$ particles is size-dependent. In particular, isotropic particles below 40 nm favor an *ac* interface. Particle morphology has a strong effect on the favored interface, as it results in some interfaces being geometrically larger than others. Thus, even when an interface is not favored for isotropic morphologies, it can become favorable for anisotropic morphologies when the high-energy interface has a sufficiently small area as compared to other interfaces. Hence, the issue of what is the lowest energy interface is determined by intrinsic factors of the material (chemical interfacial energy per unit area, elastic

constants and lattice parameters differences) as well as by extrinsic factors such as particle size and shape.

By comparing the stability of *bc*, *ac* and *ab* interfaces, our study rationalizes important qualitative features of ex situ observations of phase front orientations reported in the literature. In particular, our results are consistent with the observation of *bc* interfaces in ac-platelet micron-sized particles [11]. The energy penalty for phase-separation in large micron-sized particles is dominated by the coherency strain energy, which favors *bc* interfaces. This preference is further accentuated for *ac*-platelet particles, in which the *bc* interface is geometrically smaller than the *ac* interface. Observations of interfaces other than the *bc* interface in nano-sized particles, where chemical interfacial energy plays a larger role, are also consistent with the results our study. For particle sizes in the 100 nm – 200 nm range, several interface orientations have indeed been experimentally reported (*ac*, *bc*, *ab*, 110 and 101 [13,22,23,25,26]). Consistent with these observations, the interface orientation maps of Figure 8(a)-(c) show that the preferred interface orientation depends strongly on the particle morphology at this particle size. The *b*-needle and *bc*-platelet morphologies tend to favor *ac* interfaces, cubic, *ac*-platelet, *ab*-platelet and *a*-needle morphologies tend to favor *bc* interfaces and *c*-needle morphologies tend to favor *ab* or *bc* interfaces depending on the particle size.

An exact quantitative comparison between the predicted interface orientations of Figure 8 with experimentally observed interface orientations is challenging due to the fact that the exact particle morphology is often not reported in experimental literature.

Nevertheless, a more quantitative comparison is possible through the work of Gabrisch *et al*[23]. These authors report both *ac* and *bc* interfaces in 200 nm spherical particles, but only *bc* interfaces in micron-sized particles. As seen in Figure 8, our results suggest that *ac* interfaces could be observed in 200 nm particles that would be slightly anisotropic in the *b* and/or *c* direction, i.e. *b*-needles with L_b/L_a~2 or *bc*-platelet particles with L_a/L_c~0.5. Although not spherical, these particle morphologies are much more isotropic than the highly anisotropic micron-sized ac-platelet particles reported in the same paper (L_b/L_c~0.05, L_b/L_a~0.1), for which only *bc* interfaces were observed[23]. Our results are therefore consistent with the fact that *ac* interfaces can be observed in 200 nm particles with a low level of shape anisotropy.

An important implication of our study is that, contrary to the assumptions of many lithiation models in the literature[11,12,15,16], the *bc* interface is not always the preferred orientation in nano-sized $LiFePO_4$ particles. In particular, in the case of cubic particles, the preferred orientation was shown to be the *ac* boundary for particle sizes below 40 nm. This result is particularly relevant, as primary sizes of particles used in high-rate $LiFePO_4$ electrodes are typically on the order of 50 nm, with a certain spread on the particle size. This suggests that if lithiation of a single isotropic sub-40 nm particle were to occur under a two-phase nucleation and growth process, phase growth would actually occur in the *b* direction with the phase front oriented along the *ac* plane. In addition to being energetically favorable, this phase front orientation is also kinetically favorable, as it allows *b*-channels to be (de)lithiated simultaneously instead of being (de)lithiated sequentially.

Our study can also be extended to predict the critical size for equilibrium phase-separation in nano-particles. Several authors have attempted, using electrochemical methods[39,40] or phase field models[41], to determine the critical size at which solid solution becomes thermodynamically favorable over phase-separation in nano-particles. Based on the work by Malik et al.[17], the free energy of the non-equilibrium solid solution at room temperature is on the order of 10 meV per formula unit of Li, which corresponds to 21.5 MJ/m^3. Using the phase-separation energy of different interfaces in cubic particles as presented in Figure 4, it can be concluded that all three interface orientations (*bc*, *ac*, *ab*) are thermodynamically favored over a complete solid solution for particle sizes above 10 nm. These findings are in general agreement with the recent theoretical predictions of Ichitsubo et al[41], which state that the critical size for phase-separation is on the order of 4-10 nm. However, it should be noted that these results do not rule out a lithiation mechanism through a non-equilibrium solid solution path[17], which is by definition a mechanism that is out of thermodynamic equilibrium.

Lastly, our study can be used to determine if a thermodynamic driving force exists to form an intermediate solid solution region as an alternative to a sharp $FePO_4/LiFePO_4$ interface. Although two-phase coexistence is favored over a complete solid solution for particles larger than 10nm, Figure 3(a)-(c) show that, in a small region around the interface, the maximal value of the local coherency strain energy at a sharp $FePO_4/LiFePO_4$ interface can vary between 30-70 MJ/m^3 (depending on the interface orientation), which is higher than the free energy of the non-equilibrium solid solution

(21.5 MJ/m^3). Forming a limited intermediate solid solution region as an alternative to a sharp $FePO_4$/$LiFePO_4$ can therefore be energetically favorable, by reducing local coherency strain energy at the expense of a higher bulk free energy. This may help explain recent ex situ[25] and in situ[30] observations of intermediate solid solution regions.

In this study, we did not consider interface orientations other than the *bc*, *ac* or *ab* interfaces, and therefore no inference can be made on the incidence of higher order interfaces such as (110) and (101). Furthermore, non-cuboid particle shapes have not been considered and the interfaces were assumed to be sharp. However, the conclusions of this study are not very sensitive to the exact value of the anisotropic chemical interfacial energies. For example, even if GGA+U underestimated the *ac* chemical interfacial energy by as much as 20 mJ/m^2 (which is much larger than the ~1 mJ/m^2 numerical uncertainty associated with the DFT calculation), the crossover size between *ac* and *bc* interfaces in cubic particles would only decrease by 5 nm. This lack of sensitivity also holds for the interface orientation maps presented in Figure 8.

Conclusions

In this paper, we show using first principles calculations that the chemical interfacial energy landscape in $LiFePO_4$ is very anisotropic, with the *ac* interface having a remarkably low chemical interfacial energy with respect to the *bc* and *ab* interfaces. Because the interface orientation that minimizes the chemical interfacial energy (*ac*) is not the same as the interface orientation that minimizes the coherency strain energy (*bc*), the preferred interface orientation in $LiFePO_4$ single particles is shown to depend both on

the particle size and on the particle morphology. Our work therefore rationalizes the variety of interface orientations that have been observed in ex situ chemically delithiated particles. In particular, we show that isotropic sub-40 nm particles, which have been shown to exhibit high-rate capabilities, favor an *ac* interface. This indicates that, if such particles were to lithiate under a two-phase nucleation and growth mechanism, the preferred phase front would be oriented along the *ac* plane, and not the *bc* plane as has been assumed in most lithiation models in the literature.

Acknowledgements

This work was supported as part of the Northeastern Center for Chemical Energy Storage, an Energy Frontier Research Center funded by the US Department of Energy, Office of Science, Office of Basic Energy Sciences under Award Number DE-SC0001294. Supercomputational resources were provided by XSEDE, under grants TG-DMR97008S and TG-DMR110007. The authors would like to acknowledge Charles J. Moore, Stephen Dacek and Hui-Chia Yu for helpful comments and discussions. O. Akyildiz acknowledges support from the Scientific and Technological Research Council of Turkey, TUBITAK, through BIDEB 2219 program and no. 113F091.

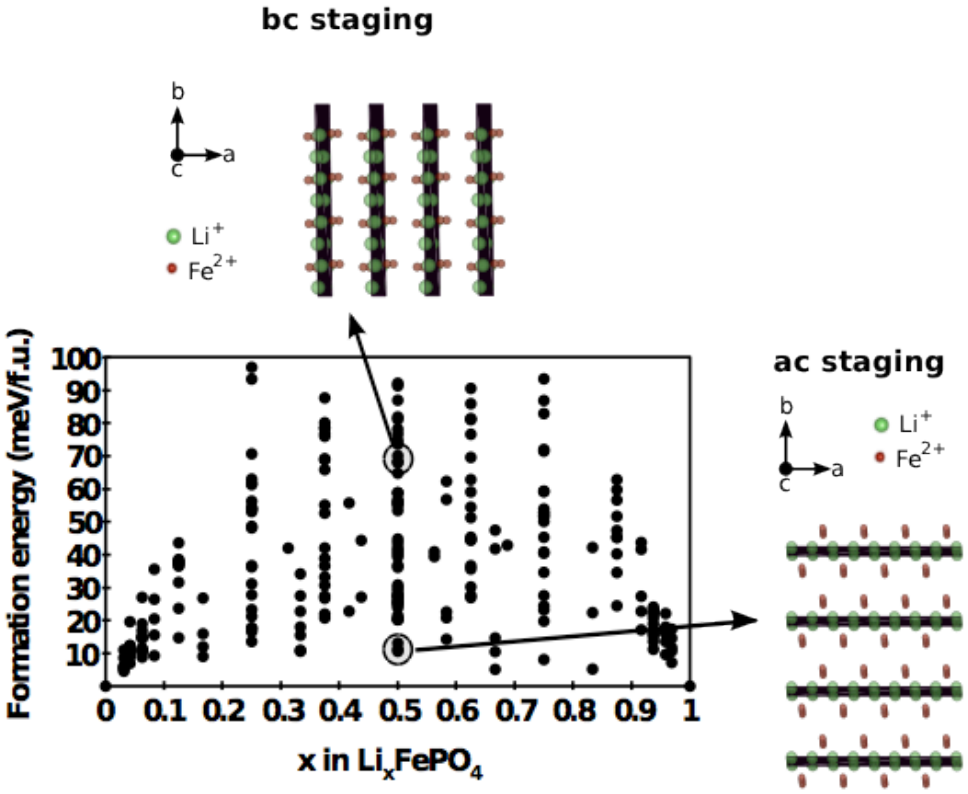

Figure 1. Energy of solid solution states calculated using GGA+U. The energy of an *ac* staging configuration (hereunto referred to as "ac ordering"), consisting in a sequence of lithiated and delithiated *ac* planes, (10 meV/f.u) is significantly lower than the energy of a *bc* staging configuration (hereunto referenced as "bc ordering"), consisting in a sequence of lithiated and delithiated *bc* planes. The formation energies of these configurations are respectively 10 meV/f.u. (*ac* ordering) and 70 meV/f.u (*bc* ordering). Because these highly ordered solid solution states are purely comprised of interfaces, this rationalizes the low value of the *ac* chemical interfacial energy with respect to the *bc* chemical interfacial energy.

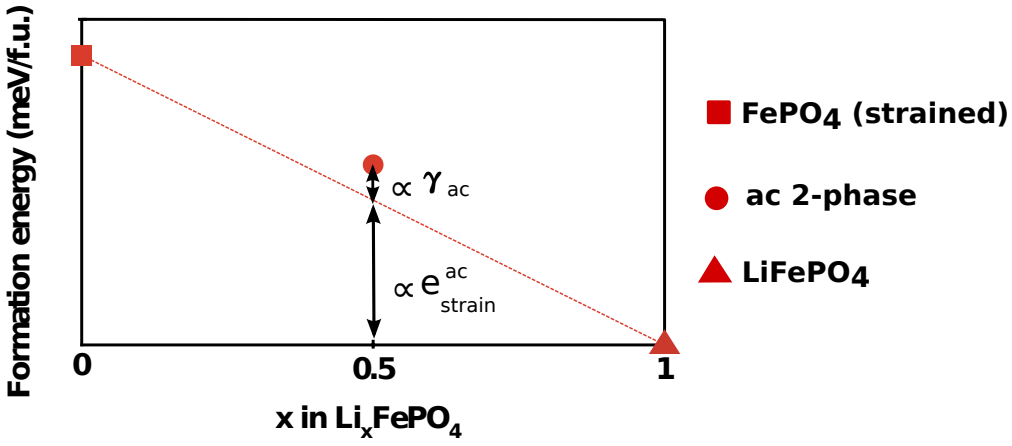

Figure 2. (a) Qualitative illustration of the *ac* chemical interfacial calculation, in the case where $LiFePO_4$ lattice parameters are imposed along the *ac* interface. The formation energies of all three configurations intervening in the chemical interfacial energy calculation (equation (3)) are positive or zero, consistent with the phase-separating character of the Li_xFePO_4 system. The coherent chemical interfacial energy is proportional to the difference between the energy of the two-phase state and the linear interpolation between the energy of the $FePO_4$ and $LiFePO_4$ phases under the lattice parameters constraint (this linear interpolation represents the coherency strain energy penalty). This energy difference is very low for an *ac* interface.

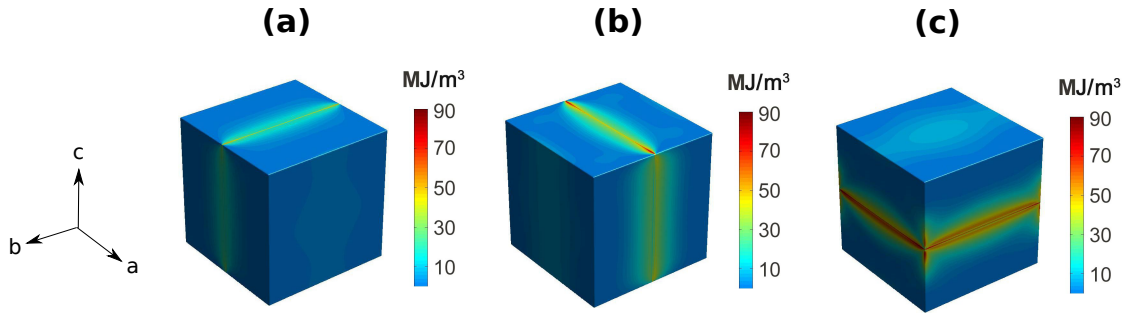

Figure 3. Color contour plots of the local coherency strain energy density for cubic particles with lithium concentration x_{Li}=*0.5*. (a) *bc* interface (b) *ac* interface (c) *ab* interface .

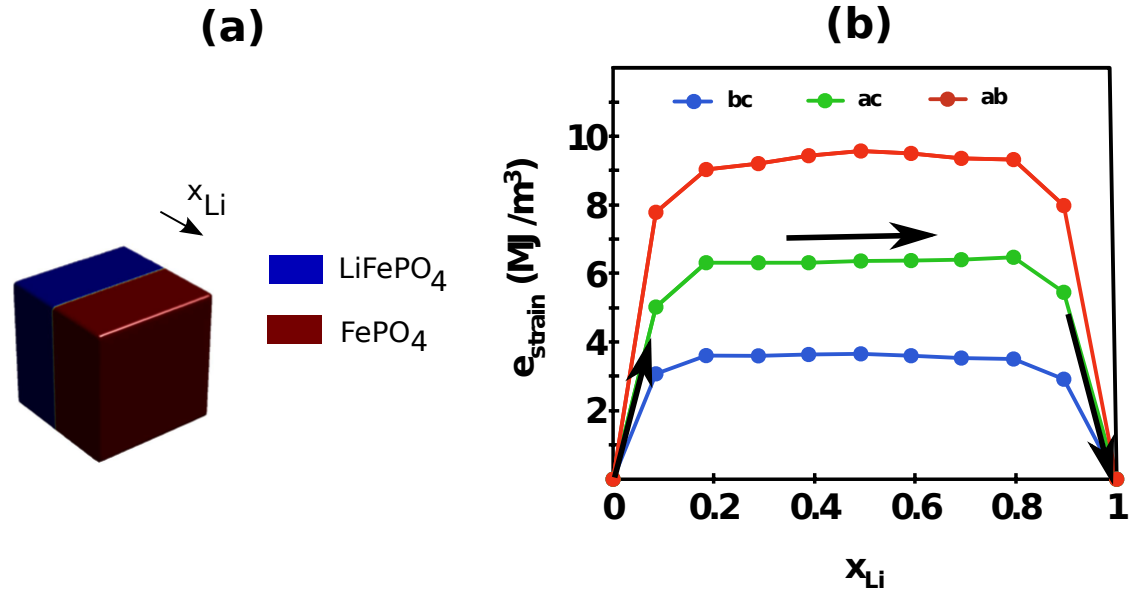

Figure 4. Variation of the volume-averaged coherency strain energy density (defined in equation (2)) with the lithium concentration at the particle level (x_{Li}) for a cubic particle. (a) Correlation between x_{Li} and the position of the interface (b) Coherency strain energy as a function of x_{Li} for *bc*, *ac* and *ab* interfaces.

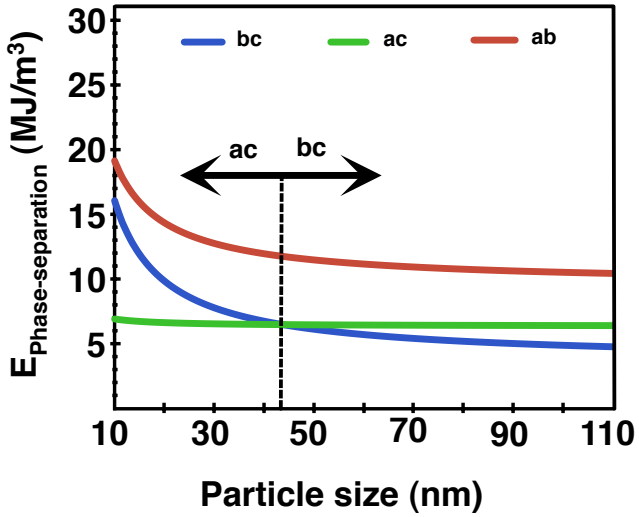

Figure 5. Total energy penalty (normalized by the particle volume) for phase-separation in a single particle as a function of the particle size for cubic particles. Each curve corresponds to a different interface orientation (*bc*, *ac* and *ab*).

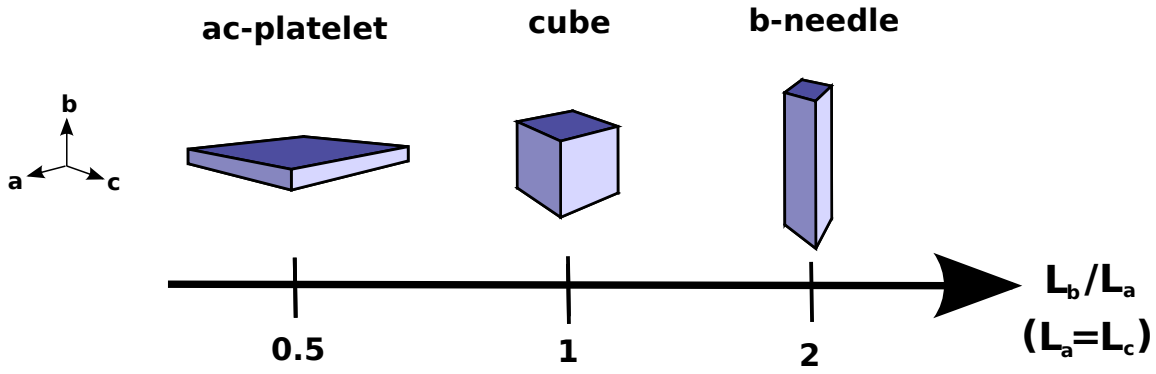

Figure 6. Morphology subspace used in Figure 7 and Figure 8(a). The lengths of the particles along the *a* and *c* directions are equal ($L_a = L_c$) while the aspect ratio L_a / L_b is allowed to vary. Three values of L_a / L_b are investigated : 0.5 (corresponding to an ac-platelet particle), 1 (corresponding to a cubic particle) and 2 (corresponding to a *b*-needle particle).

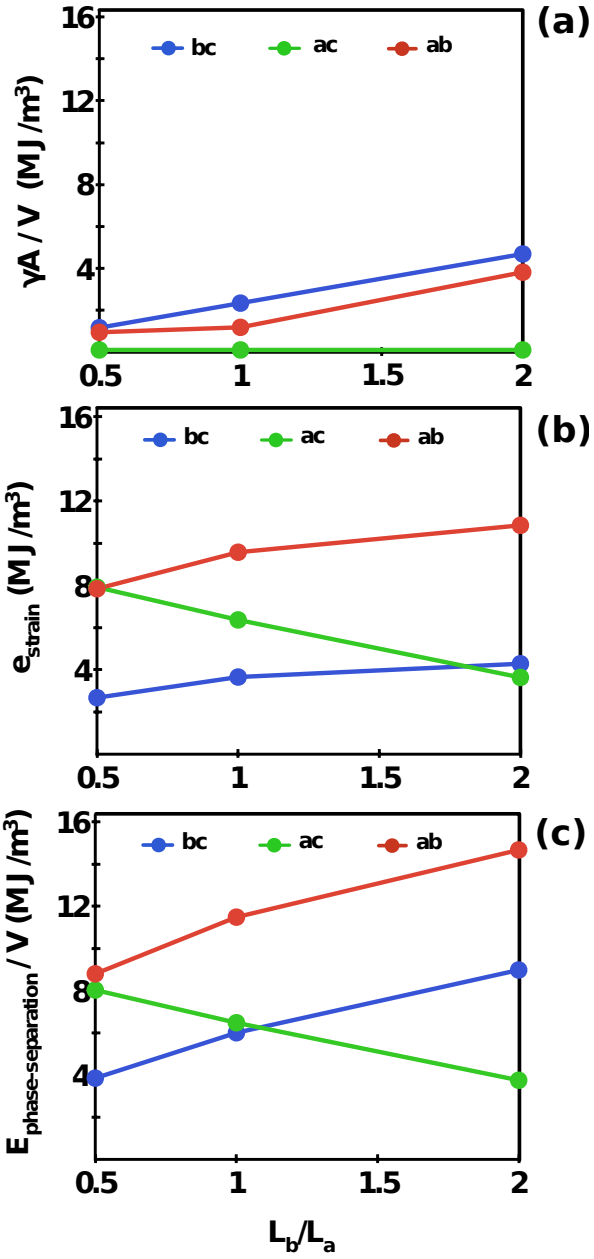

Figure 7. Effect of particle morphology on the (a) chemical interfacial energy, (b) coherency strain energy and (c) total energy penalty for phase-separation in the morphology subspace illustrated in Figure 6. A particle size of 50 nm is assumed along the *b* direction ($L_b = 50\ nm$).

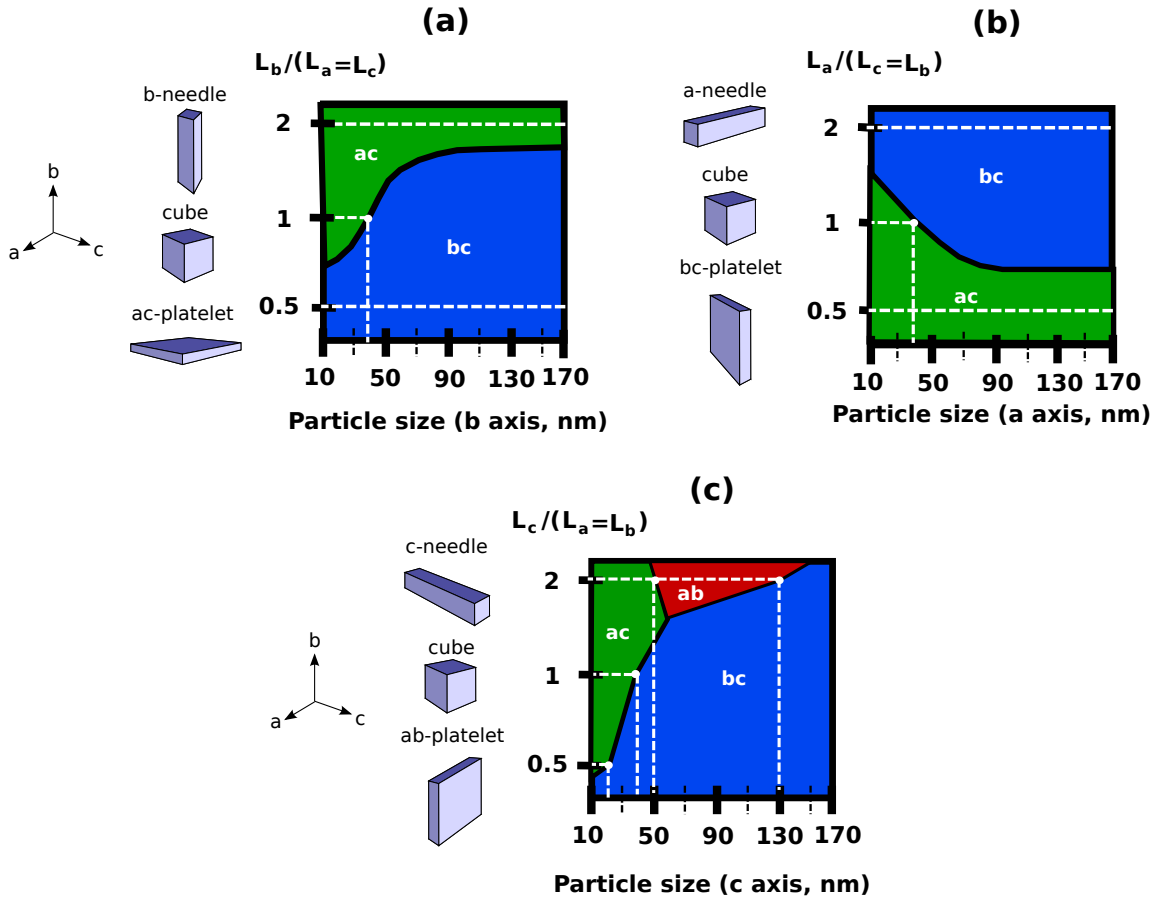

Figure 8. Qualitative interface orientation maps, displaying the favored interface orientation as a function of particle size along a certain morphology subspace. (a) Morphology subspace with $L_a = L_c$, as illustrated in Figure 6. (b) Morphology subspace with $L_c = L_b$ (c) Morphology subspace with $L_a = L_b$. In all three cases, morphology ratios of 0.5, 1 and 2 have been explicitly calculated, while intermediate morphology ratios have been qualitatively extrapolated. White dots correspond to calculated transition points, while black boundary lines represent extrapolations.

Appendix : Equations of Continuum Elasticity

Coherency strain energies are calculated using the theory of linear elasticity. The nomenclature used in linear elasticity is noted in Table 3, while the equations of linear elasticity are provided in equations (8) to (12). The corresponding boundary and continuity conditions are expressed in equations (13) and (14).

Table 3. Definition of variables used to calculate coherency strain energy

Stress tensor	Displacement vector	Total strain tensor
σ_{ij}	$\underline{u}$	ε_{ij}^{total}
Elastic strain tensor	Vegard coefficients tensor	Stiffness tensor
$\varepsilon_{ij}^{elastic}$	ε_{ij}^{0}	C_{ijkl}

Table 4. Equations of Linear Elasticity

Mechanical equilibrium	$\frac{\partial \sigma_{ij}}{\partial x_j} = 0$	(8)
Strain compatibility	$\varepsilon_{ij}^{total} = \frac{1}{2}\left(\frac{\partial u_i}{\partial x_j} + \frac{\partial u_j}{\partial x_i}\right)$	(9)
Elastic strain	$\varepsilon_{ij}^{elastic} = \varepsilon_{ij}^{total} - x_{Li}\,\varepsilon_{ij}^{0}$	(10)
Linear stress-strain relation	$\sigma_{ij} = C_{ijkl}\varepsilon_{kl}^{elastic}$	(11)
Concentration-dependent stiffness tensor (linear approximation)	$C_{ijkl}\left(x_{Li}\right) = C_{ijkl}^{FePO_4} + x_{Li}\left(C_{ijkl}^{LiFePO_4} - C_{ijkl}^{FePO_4}\right)$	(12)

Table 5. Boundary and continuity conditions

Traction free condition on the particle surface	$\sigma_{ij} \cdot n_j\big\vert_{External\ surface} = \underline{0}$	(13)
Coherency condition at the $FePO_4$/$LiFePO_4$ interface	$\underline{u}$ is continuous across the interface	(14)

Equation (8) ensures that the system is at equilibrium, equation (9) links the total strain tensor with the displacement field, equation (10) defines the elastic strain tensor as the difference between the total strain tensor and the natural strain induced by variation in lithium concentration, equation (11) expresses the linear relation between stress and elastic strain through the stiffness tensor and equation (12) expresses the concentration-dependence of the stiffness tensor. The traction-free boundary condition in equation (13) is a consequence of the fact that the external surface of the particle is traction-free, while the continuity condition in equation (14) ensures that the interface between the lithium-poor and lithium rich phases is coherent.

Values of the elastic constants for the $LiFePO_4$ and $FePO_4$ phases and values of the Vegard coefficients are taken from the first principles evaluations of Maxisch et al [27].

Bibliography

1. Zaghib, K. *et al*. Enhanced thermal safety and high power performance of carbon-coated LiFePO4 olivine cathode for Li-ion batteries. *Journal of Power Sources* **219,** 36–44 (2012).
2. Padhi, A., Nanjundaswamy, K. & Goodenough, J. Phospho-olivines as positive-electrode materials for rechargeable lithium batteries. *J Electrochem Soc* **144,** 1188–1194 (1997).
3. Huang, H., Yin, S. C. & Nazar, L. F. Approaching Theoretical Capacity of LiFePO4 at Room Temperature at High Rates. *Electrochem Solid St* **4,** A170 (2001).
4. Yamada, A., Chung, S. C. & Hinokuma, K. Optimized LiFePO4 for Lithium Battery Cathodes. *J Electrochem Soc* **148,** A224 (2001).
5. Sides, C., Croce, F., Young, V., Martin, C. & Scrosati, B. A high-rate, nanocomposite LiFePO4/carbon cathode. *Electrochem Solid St* **8,** A484–A487 (2005).
6. Yamada, A., Yonemura, M., Takei, Y., Sonoyama, N. & Kanno, R. Fast charging LiFePO4. *Electrochem Solid St* **8,** A55–A58 (2005).
7. Kang, B. & Ceder, G. Battery materials for ultrafast charging and discharging. *Nature* **458,** 190–193 (2009).
8. Islam, M. S., Driscoll, D. J., Fisher, C. A. J. & Slater, P. R. Atomic-Scale Investigation of Defects, Dopants, and Lithium Transport in the LiFePO4 Olivine-Type Battery Material. *Chem Mater* **17,** 5085–5092 (2005).
9. Chung, S.-Y., Choi, S.-Y., Yamamoto, T. & Ikuhara, Y. Atomic-Scale Visualization of Antisite Defects in LiFePO4. *Phys Rev Lett* **100,** (2008).
10. Malik, R., Burch, D., Bazant, M. & Ceder, G. Particle Size Dependence of the Ionic Diffusivity. *Nano Letters* **10,** 4123–4127 (2010).
11. Chen, G., Song, X. & Richardson, T. Electron microscopy study of the LiFePO4 to FePO4 phase transition. *Electrochem Solid St* **9,** A295–A298 (2006).
12. Delmas, C., Maccario, M., Croguennec, L., Le Cras, F. & Weill, F. Lithium deintercalation in LiFePO4 nanoparticles via a domino-cascade model. *Nat Mater* **7,** 665–671 (2008).
13. Ramana, C. V., Mauger, A., Gendron, F., Julien, C. M. & Zaghib, K. Study of the Li-insertion/extraction process in LiFePO4/FePO4. *Journal of Power Sources* **187,** 555–564 (2009).
14. Tang, M., Carter, W. C., Belak, J. F. & Chiang, Y.-M. Modeling the competing phase transition pathways in nanoscale olivine electrodes. *Electrochimica Acta* **56,** 969–976 (2010).
15. Tang, M., Belak, J. F. & Dorr, M. R. Anisotropic Phase Boundary Morphology in Nanoscale Olivine Electrode Particles. *J. Phys. Chem. C* **115,** 4922–4926 (2011).
16. Bai, P., Cogswell, D. A. & Bazant, M. Z. Suppression of Phase Separation in

LiFePO4 Nanoparticles During Battery Discharge. *Nano Letters* **11,** 1–7 (2011).
17. Malik, R., Zhou, F. & Ceder, G. Kinetics of non-equilibrium lithium incorporation in LiFePO4. *Nat Mater* **10,** 587–590 (2011).
18. Andersson, A. & Thomas, J. The source of first-cycle capacity loss in LiFePO4. *Journal of Power Sources* **97-8,** 498–502 (2001).
19. Balluffi, R. W., Allen, S. M. & Carter, C. W. *Kinetics of Materials*. 645 pages (Wiley, 2005).
20. Sun, Y., Lu, X., Xiao, R., Li, H. & Huang, X. Kinetically Controlled Lithium-Staging in Delithiated LiFePO4 Driven by the Fe Center Mediated Inter-Layer Li-Li Interactions. *Chem Mater* 121120071630001 (2012). doi:10.1021/cm3028324
21. Brunetti, G. *et al*. Confirmation of the Domino-Cascade Model by LiFePO4/FePO4 Precession Electron Diffraction. *Chem Mater* **23,** 4515–4524 (2011).
22. Laffont, L. *et al*. Study of the LiFePO4/FePO4 Two-Phase System by High-Resolution Electron Energy Loss Spectroscopy. *Chem Mater* **18,** 5520–5529 (2006).
23. Gabrisch, H., Wilcox, J. & Doeff, M. M. TEM Study of Fracturing in Spherical and Plate-like LiFePO4 Particles. *Electrochem Solid St* **11,** A25 (2008).
24. Park, S. B., Park, C. K., Hwang, J. T., Cho, W. I. & Jang, H. Anisotropic lithium ion migration in LiFePO4. *Met. Mater. Int.* **17,** 1017–1020 (2011).
25. Suo, L. *et al*. Highly ordered staging structural interface between LiFePO4 and FePO4. *Phys. Chem. Chem. Phys.* **14,** 5363 (2012).
26. Zhu, Y. *et al*. In Situ Atomic-Scale Imaging of Phase Boundary Migration in FePO 4Microparticles during Electrochemical Lithiation. *Adv. Mater.* n/a–n/a (2013). doi:10.1002/adma.201301374
27. Maxisch, T. & Ceder, G. Elastic properties of olivine LixFePO4 from first principles. *Phys. Rev. B* **73,** (2006).
28. Van der Ven, A., Garikipati, A., Kim, S. & Wagemaker, M. The Role of Coherency Strains on Phase Stability in LixFePO4: Needle Crystallites Minimize Coherency Strain and Overpotential. *J Electrochem Soc* **156,** 1–9 (2009).
29. Zhu, C. *et al*. Size-Dependent Staging and Phase Transition in LiFePO 4/FePO 4. *Adv. Funct. Mater.* n/a–n/a (2013). doi:10.1002/adfm.201301792
30. Niu, J. *et al*. In situ observation of random solid solution zone in LiFePO4 electrode. *Nano Letters* 1–24 (2014).
31. Zhou, F., Kang, K., Maxisch, T., Ceder, G. & Morgan, D. The electronic structure and band gap of LiFePO4 and LiMnPO4. *Solid State Communications* **132,** 181–186 (2004).
32. Zhou, F., Maxisch, T. & Ceder, G. Configurational electronic entropy and the phase diagram of mixed-valence oxides: The case of LixFePO4. *Phys Rev Lett* **97,** 155704 (2006).
33. Fiorentini, V. & Methfessel, M. Extracting convergent surface energies from slab calculations. *J. Phys.: Condens. Matter* **8,** 6525–6529 (1996).
34. Sun, W. & Ceder, G. Efficient creation and convergence of surface slabs. *Surface Science* **617,** 53–59 (2013).
35. Yu, H.-C., Chen, H.-Y. & Thornton, K. Extended smoothed boundary method for solving partial differential equations with general boundary conditions on complex

boundaries. *Modelling Simul. Mater. Sci. Eng.* **20,** 075008 (2012).
36. Wagemaker, M., Mulder, F. M. & Van der Ven, A. The Role of Surface and Interface Energy on Phase Stability of Nanosized Insertion Compounds. *Adv. Mater.* **21,** 2703–2709 (2009).
37. Wang, L., Zhou, F., Meng, Y. & Ceder, G. First-principles study of surface properties of LiFePO4: Surface energy, structure, Wulff shape, and surface redox potential. *Phys. Rev. B* **76,** 165435 (2007).
38. Cogswell, D. A. & Bazant, M. Z. Coherency Strain and the Kinetics of Phase Separation in LiFePO 4Nanoparticles. *ACS Nano* **6,** 2215–2225 (2012).
39. Meethong, N., Huang, H.-Y. S., Carter, W. C. & Chiang, Y.-M. Size-Dependent Lithium Miscibility Gap in Nanoscale Li1-xFePO4. *Electrochem Solid St* **10,** A134 (2007).
40. Kobayashi, G. *et al*. Isolation of Solid Solution Phases in Size-Controlled LixFePO4 at Room Temperature. *Adv. Funct. Mater.* 395–403 (2009).
41. Ichitsubo, T. *et al*. What determines the critical size for phase separation in LiFePO4 in lithium ion batteries? *J. Mater. Chem. A* (2013). doi:10.1039/c3ta13122j

Graphic and One Sentence Summary

Using calculations based on first principles, we demonstrate that the preferred interface in singles $LiFePO_4$ particles depends both on the particle size and morphology.